Electronic Supplementary Material (ESI) for EES Catalysis.

Pathways to Enhance Electrochemical CO_2 Reduction Identified Through Direct Pore-Level Modeling

Supplementary Information

Evan F. Johnson, Etienne Boutin, Shuo Liu, Sophia Haussener
2023

S1 Homogeneous Reaction Equations

The source term R_i of homogeneous reactions in the GMPNP formulation (Eq. 1) are as follows, where k is the rate constant and C is the species concentration.

$$R_{K^+} = 0 \tag{S1}$$

$$R_{HCO_3^-} = -k_{1f} C_{OH^-} C_{HCO_3^-} - k_{2r} C_{HCO_3^-} + k_{1r} C_{CO_3^{2-}} + k_{2f} C_{CO_2} C_{OH^-} \tag{S2}$$

$$R_{CO_2} = -k_{2f} C_{CO_2} C_{OH^-} + k_{2r} C_{HCO_3^-} \tag{S3}$$

$$R_{CO} = 0 \tag{S4}$$

$$R_{H^+} = -k_{w2} C_{H^+} C_{OH^-} + k_{w1} \tag{S5}$$

$$R_{OH^-} = -k_{w2} C_{H^+} C_{OH^-} - k_{1f} * C_{OH^-} C_{HCO_3^-} - k_{2f} C_{CO_2} C_{OH^-} + k_{w1} + k_{1r} C_{CO_3^{2-}} + k_{2r} C_{HCO_3^-} \tag{S6}$$

$$R_{CO_3^{2-}} = -k_{1r} C_{CO_3^{2-}} + k_{1f} C_{OH^-} C_{HCO_3^-} \tag{S7}$$

$$R_{H_2} = 0 \tag{S8}$$

S2 Tafel Parameterization

A 1D version of the GMPNP model was run for a flat cathode immersed in electrolyte to match the planar electrode setup of Hatsukade et al.[1] The current density and potential from that study are specified in the 1D GMPNP model, and the model solves for the CO_2 concentration at the OHP. Plotting the concentration-normalized current density (the experimentally found CO current divided by the modeled CO_2 concentration at the OHP), two different regions are evident, as shown in Fig. S1. The parameters for both regions are given in Table S1. The dashed line shows the continuation of the 120 mV/dec line, indicating that neglecting the change in Tafel slope results in a vast overestimation of CO current density at potentials lower than -1.1 V. The difference is roughly two orders of magnitude at -1.4 V, which likely contributes to the extremely high CO currents predicted by previous models[2] (see Fig. S11). The R^2 values shown are for the linearized graph (i.e. they are calculated after taking the log of the CO current).

No surface roughness was reported along with the experimental data set used for this parameterization,[1] so it is assumed that the reported current densities are normalized by the geometric area. Similar to previous modeling studies parameterised with the same data set,[2,3] we use the experimental current densities without modification for the surface roughness. This is a valid assumption if the smooth catalyst surfaces depicted in this study are actually assumed to have some additional surface roughness similar to the surface in the experiment.

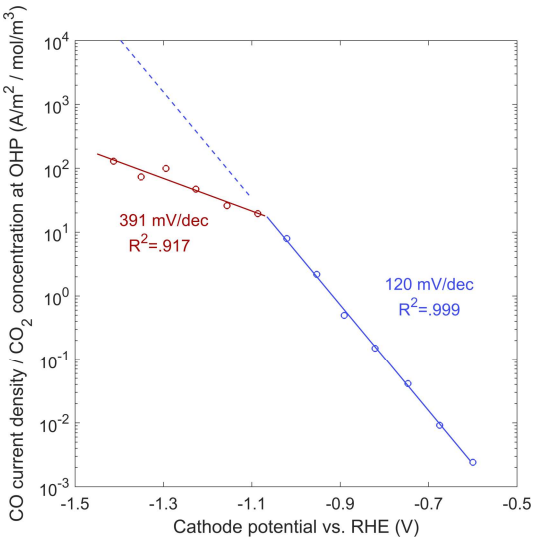

Figure S1 CO current density divided by CO_2 concentration at the OHP, showing the Tafel fit over two distinct regions, as implemented in the transport model. The dashed line indicates the continuation of the 120 mV/dec line, showing how the Tafel parameterization would look if only the data points from -0.6 to -1.0 V were used for parameterization.

S3 Mixture-Average Diffusion

In the gaseous domain, transport of CO_2, CO, and H_2 is due to both diffusion of species and convection of the bulk fluid mixture (Eq. S9). The first term represents multicomponent diffusion, where the diffusive flux is modeled with Mixture Averaged Diffusion (MAD).[4] ω_i is the mass fraction of species i, M is the molar mass, and ρ is the mixture density. This formulation takes into account both Maxwell (D_i^{m}) and Knudsen diffusion (D_i^{K}), which are combined in Eq. S13, and corrected for porosity (ε_m) using the Bruggerman relationship with the factor $\varepsilon_m^{3/2}$. The Knudsen diffusion coefficient is found from kinetic gas theory in Eq. S12. The second term in Eq. S9 accounts for convection, with the mixture velocity (u) found with Darcy's Law (Eq. S15), which solves for the pressure drop

using the permeability (κ) and viscosity (μ). In the DM, the permeability, mean pore diameter, and porosity are chosen as those of the commercially available carbon GDE Sigracet GDL 35 BA, measured by El-kharouf et al.,[5] and the mean free path (λ_{path}) is taken as the mean pore diameter. In the gaseous region around the catalyst particles, the porosity is 1, and the mean free path is the narrowest gaseous gap between two particles in the y-direction. Since Darcy's law uses the permeability, an innately porous property, but we wish to resolve the species transfer as if it were open (non-porous) in the gaseous region around the catalyst particles, the permeability is taken as an order of magnitude higher than the permeability in the DM. These properties along with the Maxwell diffusion constants are given in Table S1.

$$\nabla \cdot \vec{J}_i + \rho(\vec{u} \cdot \nabla)\omega_i = R_i \tag{S9}$$

$$\vec{J}_i = -\left(\rho D_i^{\mathrm{mK}} \nabla \omega_i + \rho \omega_i D_i^{\mathrm{mK}} \frac{\nabla M_{\mathrm{n}}}{M_{\mathrm{n}}} - \rho \omega_i \sum_k \frac{M_i}{M_n} D_k^{\mathrm{m}} \nabla x_k\right) \tag{S10}$$

$$D_i^{\mathrm{m}} = \frac{1-\omega_i}{\sum_{k \neq i} \frac{x_k}{D_{ik}}} \tag{S11}$$

$$D_i^{\mathrm{K}} = \frac{\lambda_{path}}{3}\sqrt{\frac{8RT}{\pi M_i}} \tag{S12}$$

$$D_i^{\mathrm{mK}} = \varepsilon_m^{3/2}\left(\frac{1}{D_i^m} + \frac{1}{D_i^K}\right)^{-1} \tag{S13}$$

$$M_{\mathrm{n}} = \left(\sum_i \frac{\omega_i}{M_i}\right)^{-1} \tag{S14}$$

$$\vec{u} = -\frac{\kappa}{\mu}\nabla p \tag{S15}$$

S4 Additional Results

Contour plots are shown in Fig. S2 for the 50%-wetted case. Concentrations are much more uniform throughout the catalyst layer than the 50%-filled case, as the liquid-gas interface extends along the entire film. The CO_2 concentration is nearly uniform, though it is around 18 mM, well below the 34 mM which would be the concentration at the interface in pure water. This is caused by the reduction in solubility due to high ionic concentrations.

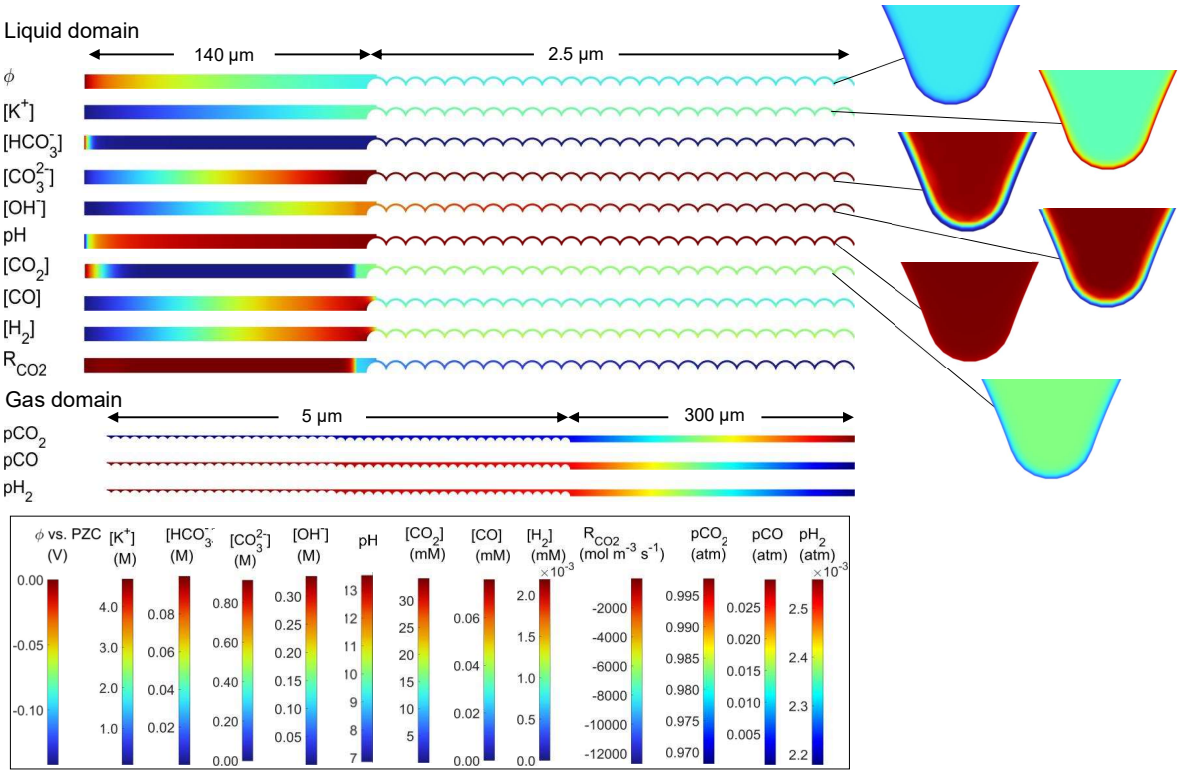

Figure S2 Potential, concentrations, and partial pressures for the 50%-wetted case with a cathode potential of -1.1 V vs. RHE and a 0.1 M $KHCO_3$ electrolyte.

The Henry's constant, averaged along the liquid-gas interface, is shown in Figure S3. The solubility is significantly reduced from the pure water value of 34 mM due to the ionic strength of the electrolyte, modeled with the Sechenov relation. The 100%-filled configuration shows has lowest solubility at each potential, as resistance to diffusion is highest, causing the most accumulation of OH^- and CO_3^{-2}.

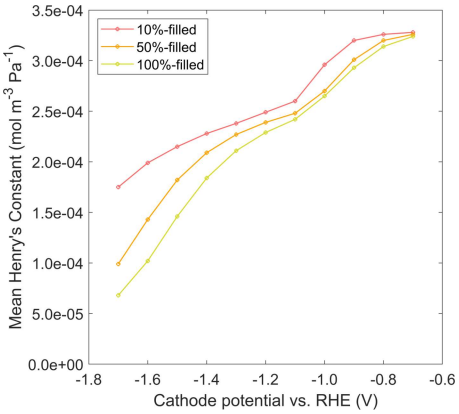

Figure S3 Average Henry's constant along the liquid-gas interface for the three filled configurations.

The FE_{CO} averaged on each nanoparticle is shown in Fig. S4 for all six wetting configurations. In the filled configurations, as more negative potentials are applied, the particles near the liquid-gas interface remain high, but the deepest particles become to be suppressed. Thus, it is first the deepest particles which bring down the overall FE_{CO} in Fig. 7(b). The FE_{CO} in the wetted configuration is essentially uniform across the catalyst layer, but it peaks at -1.1 V in all wetted cases.

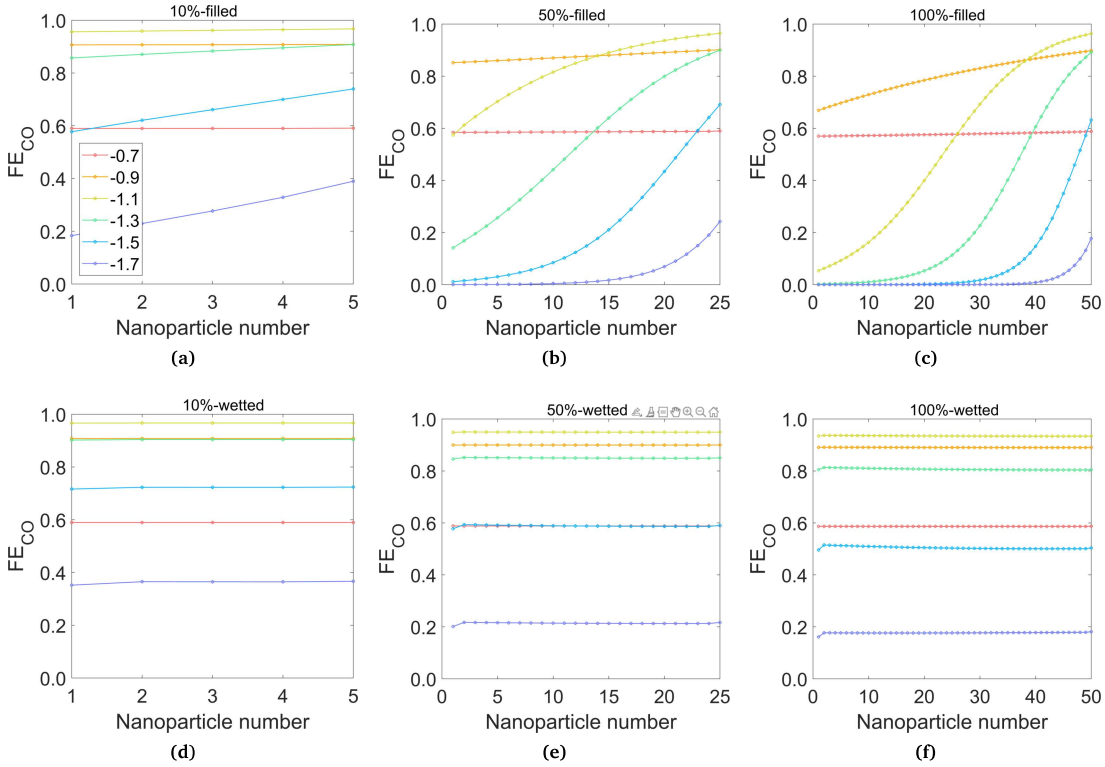

Figure S4 Mean FE_{CO} at the surface of each nanoparticle for the six wetting cases. Nanoparticles are numbered starting at 1 for the left-most (deepest) particle.

S5 Sechenov Relation in CO_2R Literature

The Sechenov relation dates originally from 1889,[6] but later Weisenberger and Schumpe[7] used many experimental results to find the fitting parameters for Eq. S16. $H_{i,0}$ and H_i are the gas solubilities in pure water and the electrolyte, respectively, and C_j is the ion

concentration. The parameters they solved for are h_j and $h_{g,i}$ for the ionic and gaseous species, respectively. Temperature effects are also considered,[7] but are neglected in the present analysis.

$$\log(H_{i,0}/H_i) = \sum_{j=1}^{n_{ionv}} \left(h_j + h_{g,i}\right) C_j \tag{S16}$$

This equation is rearranged to solve for the modified Henry's constant H_i in Eq. 17. In CO_2R literature, this notation matches Burdyny et al.[8] (details shown in SI of cited paper). Blake et al.[3] (also shown in SI of the cited paper) use an equation with e instead of 10 as the base of the exponential function ($H_i = H_{i,0} \prod_j e^{-h^j c^j}$), using the same parameters from Weisenberger and Schumpe. However, this form does not match the form of Eq. S16, for which the parameters were derived. One possible explanation is the ambiguity of the term log, which is usually taken to mean base 10 in engineering but base e in other fields. However, any ambiguity is clarified by following the example calculation by Weisenberger and Schumpe.[7] They intend the log to be base 10, leading to the form shown in this paper.

S6 Size Reduction with x-coordinate Transformation

The x-coordinate transformation is performed to reduce the size of the domain outside of the catalyst layer by a factor F_R. After assuming steady state conditions, substituting the flux equation (Eq. 2) into the species balance equation (Eq. 1), and substituting $x \rightarrow F_R x$, the GMPNP equations in the x direction are given in Eq. S17-S18.

$$0 = -\frac{1}{F_R}\frac{\partial}{\partial x}\left(-\frac{D_i}{F_R}\frac{\partial C_i}{\partial x} - \frac{D_i C_i z_i F}{RTF_R}\frac{\partial \phi}{\partial x} - \frac{D_i C_i}{F_R}\left(\frac{N_A \sum_{j=1}^{n} a_j^3 \frac{\partial C_j}{\partial x}}{1 - N_A \sum_{j=1}^{n} a_j^3 C_j}\right)\right) + \sum_p R_i \tag{S17}$$

$$\frac{1}{F_R}\frac{\partial}{\partial x}\left(\frac{\varepsilon_0 \varepsilon_r}{F_R}\frac{\partial \phi}{\partial x}\right) = -F\sum_{i=1}^{n} z_i C_i \tag{S18}$$

From Eq. S17-S18, if the effective properties shown in Eq. S19-S22 are substituted, then we arrive back at the original GMPNP equation. (The right side of the Poisson equation (Eq. 3) is $F\sum_{i=1}^{n} z_i C_i$, representing the charge density, ρ_v, used in Eq. S22.) Thus, the coordinate transformation can be implemented in two different ways, either by implementing the modified governing equations (Eq. S17-S18) in the domain to transform, or by keeping the original governing equations throughout the entire domain and using these effective properties in the transformed domain. The latter method is used in the present implementation. Note that by using these effective properties, one F_R stays inside the flux term, and one F_R stays outside (or is brought to the other side of the equation), which is important to ensure the flux is calculated correctly. In general, the effective properties should be applied anisotropically because only the x coordinate is transformed, however, isotropic properties are used in this model as there is no flux in the y-direction in the transformed regions. Similarly, the effective properties used to transform the gaseous domain (MAD+Darcy's law) are given in Fig. S23-S25.

$$D_{i,eff} = D_i/F_R \tag{S19}$$

$$\varepsilon_{r,eff} = \varepsilon_r/F_R \tag{S20}$$

$$R_{i,eff} = R_i F_R \tag{S21}$$

$$\rho_{v,eff} = \rho_v F_R \tag{S22}$$

$$D^m_{i,eff} = D^m_i/F_R \tag{S23}$$

$$D^K_{i,eff} = D^K_i/F_R \tag{S24}$$

$$\kappa_{eff} = \kappa/F_R \tag{S25}$$

S7 Verification

For verification that the size reduction transformation was implemented properly, separate (not coupled) simulations were run for both the liquid (GMPNP) domain and for the gaseous (MAD + Darcy's Law) domains. This allows for a simple comparison in each domain to ensure the scaling has been implemented correctly.

To verify the scaling of the gaseous domain, a rectangular domain of length 30 μm was used. In MAD, mass fractions were specified at the gas supply stream (right side of rectangular domain) to be (arbitrarily) 0.01, 0.01, and 0.98 for CO, H_2, and CO_2 respectively. On the left side, representing what would be the interface in a coupled simulation, mass fluxes were arbitrarily specified to be 0.01, 0.15, and 0.02 mol m^{-2} s^{-1} for CO, H_2, and CO_2 respectively. Darcy's Law boundary conditions are a pressure of 1 atm on the gas supply (right) side. On the opposite (left) side, a mass flux boundary condition was specified as the summation of the molar fluxes, as specified in the actual model. On the top and bottom, zero flux boundary conditions were applied, so the model is run in 2D, but there is no flux in the y-direction.

The original simulation is run for a 30 μm domain, with unmodified MAD and Darcy's Law equations. Then a factor of F_R=10 is applied, by reducing the length to 3 μm and applying the effective properties in Eq. S19 to S25. Results are shown in Fig. S5, where the mass fractions from the original simulation are plotted against the distance from the gas supply stream, while the size-reduced simulation is plotted against the distance multiplied by 10. A perfect match is seen in the results, showing the transformation as been implemented correctly.

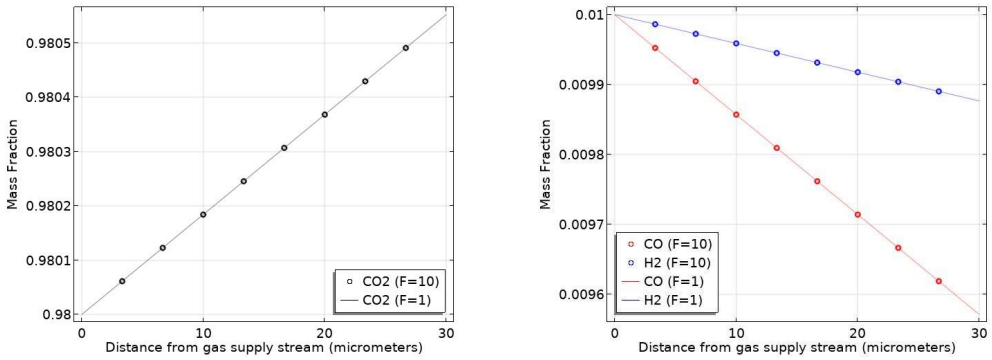

(a) (b)

Figure S5 Comparison of unmodified (lines) and reduced size region with F_R=10 (circles) in a gas domain, showing mass fraction of (a) CO_2, and (b) CO and H_2.

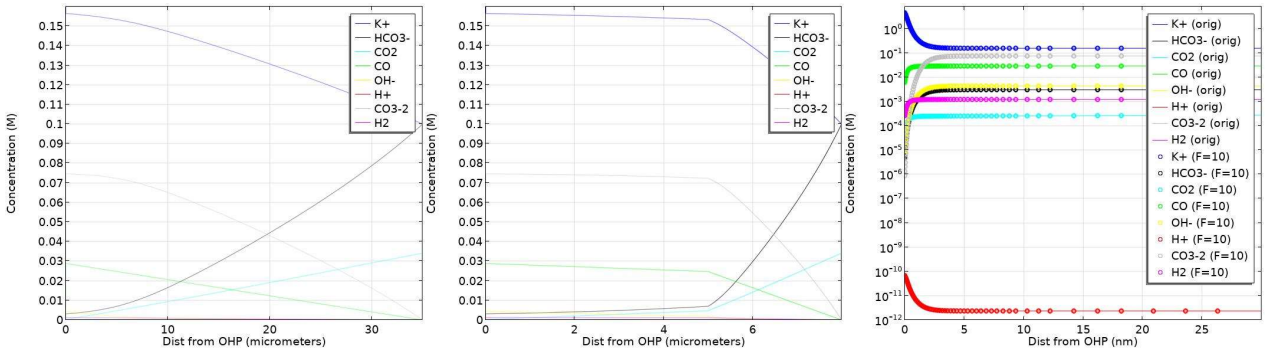

(a) (b) (c)

Figure S6 Verification of x-transformation for GMPNP, showing concentrations for (a) the original unmodified domain, (b) the domain reduced in size with F_R=10 between 5 and 35 µm, and (c) a comparison of results between the original (lines) and reduced domains (circles) near the cathode surface.

For verification of the transformation of the GMPNP equations, the original domain is 35 μm in length. The transformed domain consists of a 5 μm section near the cathode which is not reduced in size, next to a 3 μm section with F_R=10, representing the remaining 30 μm. Fig. S6(a) and (b) show the results for the original domain and the reduced domain, respectively. The two plots show the same results from 0 to 5 μm, and at higher distances the reduced version shows the same data as the original, but squeezed into a span of 3 μm instead of 30 μm. Fig. S6(c) shows a direct comparison of the results near the cathode surface. The original and the modified (F_R=10) cases are identical, verifying the transformation is correct.

S8 Electric Double Layer Theory

We follow the electric double layer theory and terminology as described by Newman and Thomas-Alyea [9] and Bard and Faulkner. [10] The first layer is formed by the Inner Helmholtz Plane (IHP), which is defined by the center of specifically adsorbing (not fully hydrated) ions, which is also referred to as the "compact" or "Stern" layer. In the current model, no ions are considered to be specifically adsorbed, as cations under these conditions typically do not specifically adsorb, and anions are repelled from the cathode at moderate potentials. Therefore, the Stern/compact/IHP is not included explicitly in the model. The outer Helmholtz plane (OHP) is formed by the centers of the hydrated cations. In the "diffuse layer", the electrolyte is not electroneutral (there is "charge separation") due to the repulsion of anions and attraction of cations to the cathode. The region is only 1-10 nm in thickness, and there are strong concentration gradients. In the "diffusion layer", electroneutrality is observed, but there are still concentration gradients. In the bulk, there are no concentration gradients, and there is electroneutrality.

The GMPNP formulation models the diffuse and diffusion layers with the fluxes given in Eq. 2. The region in between the metal cathode surface and the OHP is assumed to have a linear potential drop, since there are no charged ions in this region. This potential

drop is due to the capacitance between the metal and the OHP, modeled with the boundary condition in Eq. 9. The capacitance is the permittivity of this region divided by distance, where the value used (20 μF cm^{-2}) corresponds to the experimentally found value for the capacitance of this region. Thus, with an applied potential, part of the potential drop is between the metal and the OHP, and part is from the OHP to the bulk. Many previous models assume electroneutrality applies throughout the modeled domain, which amounts to neglecting the diffuse layer altogether. Instead of assuming electroneutrality, in this work the Poisson equation is used to model charge separation.

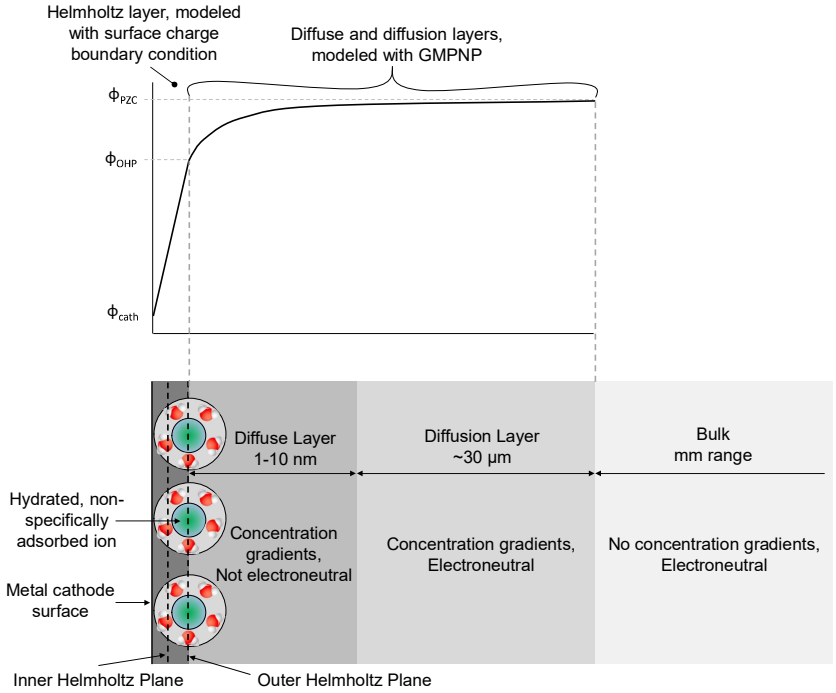

Figure S7 Schematic of the electric double layer in 1D[9] and corresponding potential profile.

The original PNP model neglects any steric ("crowding") effects. The result is that the calculated cation concentration at the OHP can become unrealistically large. Including the steric term limits the maximum concentration possible on the surface to a more realistic value. The GMPNP model includes a term to account for steric effects, given in Eq. 2. To demonstrate the difference between PNP (no steric term) and GMPNP (with steric term), Fig. S8 shows the cation concentration calculated with both models in 1D. The GMPNP model reduces the cation concentration at the OHP, keeping it below the fully packed steric limit of 5.73 M (based on a K^+ solvation diameter of 0.662 nm). The PNP model reaches concentrations above 16 M at a potential of -1.6 vs RHE. At even more negative applied potentials the PNP model has difficulty converging, as the concentration at the OHP reaches excessively high values.

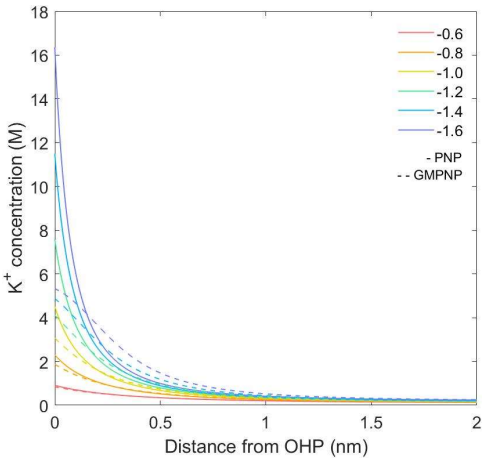

Figure S8 Comparison of results between models: GMPNP (with steric term) and PNP (without steric term).

S9 pH Dependence on the Tafel Equations

Some studies have noted a pH dependence on HER. The relevant pH is at the reaction plane (the OHP). The strong attraction of cations and repulsion of anions, along with the OH^- produced and steric effects cause the high gradients in pH and pOH, visible in the 1D GMPNP results shown in Fig. S9. Note that care should be taken when referring to the pH, as H^+ and OH^- are not in equilibrium (their sum is not necessarily 14), so their concentrations at the OHP can be considered independent parameters for modeling, as each may have their own effect on the reaction (or not). In the figure, pH is $-\log[H^+]$ and pOH is $-\log[OH^-]$.

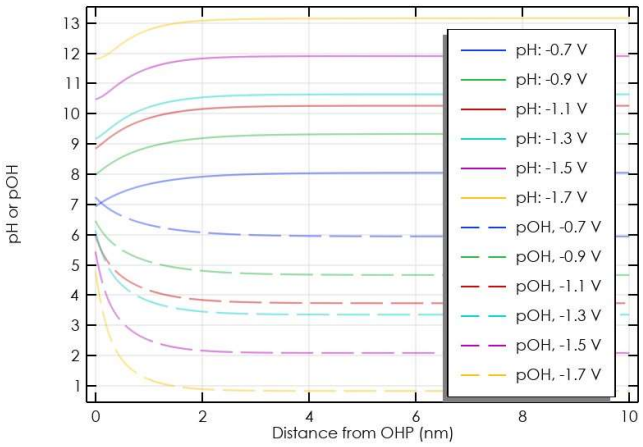

Figure S9 1D GMPNP model results, showing pH and pOH near the OHP (the diffuse layer).

Experimental HER results from Zheng et al. are reproduced in Fig. S10, covering four different catalysts.[11] Each catalyst was tested with several electrolytes to cover a wide pH range. Referring to Fig. S10(a), there is certainly a pH dependence in the acidic region, with a roughly linear dependence when plotted on a log scale, as described by Zheng et al. This matches the expectation that HER should be dependent on the H^+ concentration, which has been modeled using a Tafel equation weighted by H^+ concentration at the OHP.[2,12]

However, focusing only on the data in the basic region and plotting the same data on linear axes, shown in Fig. S10(b), there is no downward trend visible. That is, the exchange current density of HER is not suppressed at higher pH values in the range of 7 to 14. This agrees well with the assumption made that HER depends on the H^+ concentration in the acidic range, but not in a basic medium when H_2 is generated by splitting water, which is always in abundance. Since it is still a topic of debate in literature and experimental evidence does not clearly show HER suppression in a basic medium, no pH dependence at the OHP is considered in the model.

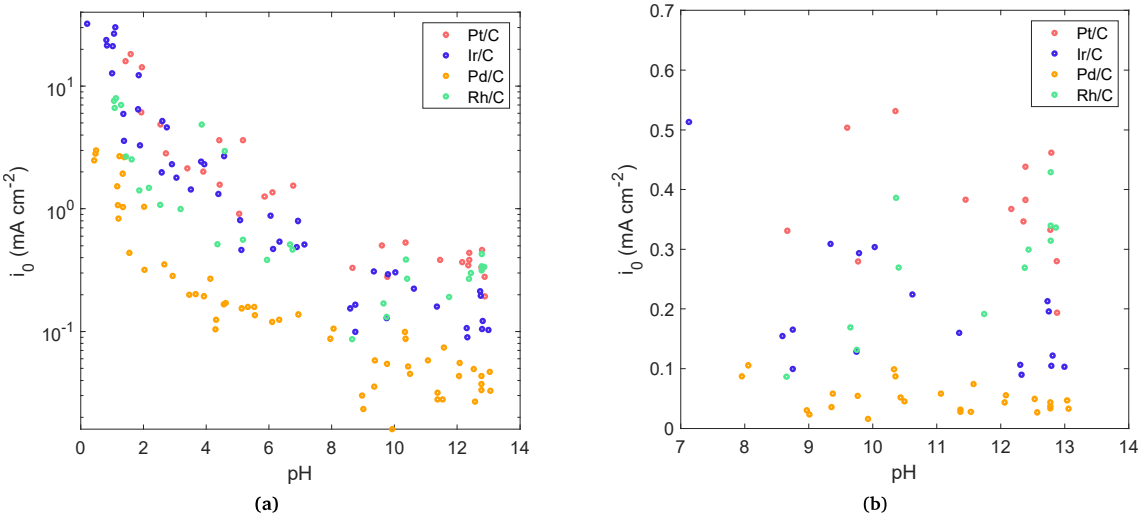

Figure S10 HER exchange current density dependence on pH, reproduced from Zheng et al.[11], showing (a) data from the full pH range, and (b) the same data but close-up on the basic region plotted on linear axes.

S10 Comparison of Results to 1D Volume-Averaged Model

The results from Weng et al.[2] are digitally reproduced and shown along with the experimental data and modeling results from the present study. When plotted with a linear (not log) y-axis, it is clear the 1D volume-averaged model results are quite high: roughly an order of magnitude higher than experimental results at -1.2 V vs. RHE, and likely 2 orders of magnitude higher if experiments were run as low as -1.7 V vs. RHE.

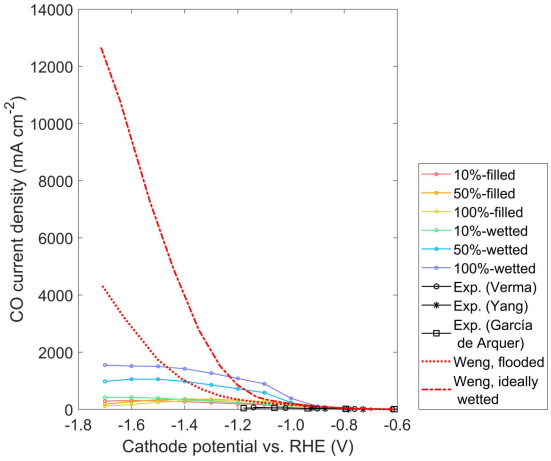

Figure S11 CO current density with same cases as Fig. 7, including results digitally reproduced from Weng et al.[2]

S11 Parameters Used in Model

Table S1 Aqueous phase parameters

Parameter	Value	Unit	Ref.
Steric Diameters			
a_{K^+}	0.662	nm	13
$a_{HCO_3^-}$	0.800	nm	13
a_{CO_2}	0.230	nm	13
a_{CO}	0.113	nm	13
a_{H^+}	0.560	nm	13
a_{OH^-}	0.600	nm	13
$a_{CO_3^{2-}}$	0.788	nm	13
Bulk Electrolyte Concentrations			
C_{K^+}	0.10	M	13
$C_{HCO_3^-}$	0.09992	M	13
C_{CO_2}	0.034061	M	13
C_{CO}	0.0	M	13
C_{H^+}	1.4E-07	M	13
C_{OH^-}	7.1E-08	M	13
$C_{CO_3^{2-}}$	3.90E-05	M	13
C_{H_2}	0.0	M	13
Aqueous Phase Diffusivities			
D_{K^+}	1.957E-9	$m^2\ s^{-1}$	13
$D_{HCO_3^-}$	1.185E-9	$m^2\ s^{-1}$	13
D_{CO_2}	1.910E-9	$m^2\ s^{-1}$	13
D_{CO}	2.030E-9	$m^2\ s^{-1}$	13
D_{H^+}	9.311E-9	$m^2\ s^{-1}$	13
D_{OH^-}	5.273E-9	$m^2\ s^{-1}$	13
$D_{CO_3^{2-}}$	9.230E-10	$m^2\ s^{-1}$	13
D_{H_2}	4.875E-9	$m^2\ s^{-1}$	13
Homogeneous Reaction Rate Constants			
k_{w1}	2.40E-2	$mol\ m^{-3}\ s^{-1}$	13
k_{w2}	2.40E+6	$m^3\ mol^{-1}\ s^{-1}$	13
k_{1f}	6.00E+6	$m^3\ mol^{-1}\ s^{-1}$	13
k_{1r}	1.07E+6	s^{-1}	13
k_{2f}	2.23	$m^3\ mol^{-1}\ s^{-1}$	13
k_{2r}	5.23E-5	s^{-1}	13
Tafel Parameters, CO_2, for $\phi_{c,RHE}$<-1.07			
$i_{0,CO}$	0.062969	$A\ m^{-2}$	
α_{CO}	0.151187	-	
Tafel Parameters, CO_2, for $\phi_{c,RHE}$>-1.07			
$i_{0,CO}$	1.8688E-7	$A\ m^{-2}$	
α_{CO}	0.493018	-	
Tafel Parameters, H_2			
i_{0,H_2}	0.00109428	$A\ m^{-2}$	
α_{H_2}	0.203468	-	

Table S2 Gas phase parameters

Parameter	Value	Unit	Ref.
Diffusivities			
D_{H_2-CO}	0.743	$cm^2\ s^{-1}$	2
$D_{H_2-CO_2}$	0.646	$cm^2\ s^{-1}$	2
D_{CO-CO_2}	0.152	$cm^2\ s^{-1}$	2
Material Properties			
Porosity, DM	0.705	-	5
Permeability, DM (κ)	5.31E-11	m^2	5
Pore diameter, DM (λ_{path})	2469	nm	5
Porosity, around catalyst particles	1	-	-
Permeability, around catalyst particles (κ)	5.31E-10	m^2	5
Pore diameter, around catalyst particles (λ_{path})	20	nm	-

Table S3 Henry's constants and Sechenov relation parameters, corresponding to Eq. 17

Parameter	Value	Unit	Ref.
Henry's Constants in Pure Water			
$H_{CO_2,0}$	3.40E-4	$mol\ m^{-3}\ Pa^{-1}$	14
$H_{CO,0}$	9.70E-6	$mol\ m^{-3}\ Pa^{-1}$	14
$H_{H_2,0}$	7.80E-6	$mol\ m^{-3}\ Pa^{-1}$	14
Electrolyte Parameters			
h_{K^+}	0.0922	M^{-1}	7
$h_{HCO_3^-}$	0.0967	M^{-1}	7
h_{OH^-}	0.0839	M^{-1}	7
$h_{CO_3^{2-}}$	0.1423	M^{-1}	7
Gas Parameters			
h_{g,CO_2}	-0.0172	M^{-1}	7
h_{g,H_2}	-0.0218	M^{-1}	7

References

[1] T. Hatsukade, K. P. Kuhl, E. R. Cave, D. N. Abram and T. F. Jaramillo, *Phys. Chem. Chem. Phys.*, 2014, **16**, 13814–13819.

[2] L.-C. Weng, A. T. Bell and A. Z. Weber, *Physical Chemistry Chemical Physics*, 2018, **20**, 16973–16984.

[3] J. Blake, J. Padding and J. Haverkort, *Electrochimica Acta*, 2021, **393**, 138987.

[4] L. Cussler, *Multicomponent Diffusion*, Elsevier Scientific Publishing Company, 1976.

[5] A. El-kharouf, T. J. Mason, D. J. Brett and B. G. Pollet, *Journal of Power Sources*, 2012, **218**, 393–404.

[6] J. Setschenow, *Zeitschrift für Physikalische Chemie*, 1889, **4U**, 117–125.

[7] S. Weisenberger and A. Schumpe, *AIChE Journal*, 1996, **42**, 298–300.

[8] T. Burdyny, P. J. Graham, Y. Pang, C.-T. Dinh, M. Liu, E. H. Sargent and D. Sinton, *ACS Sustainable Chemistry & Engineering*, 2017, **5**, 4031–4040.

[9] J. Newman and K. Thomas-Alyea, *Electrochemical Systems*, 3rd edn, 2004.

[10] A. J. Bard and L. R. Faulkner, *Electrochemical methods: fundamentals and applications*, Wiley, New York, 2nd edn, 2001.

[11] J. Zheng, W. Sheng, Z. Zhuang, B. Xu and Y. Yan, *Science Advances*, 2016, **2**, e1501602.

[12] J. Gu, S. Liu, W. Ni, W. Ren, S. Haussener and X. Hu, *Nature Catalysis*, 2022, **5**, 268–276.

[13] D. Bohra, *PhD thesis*, TU Delft.

[14] R. Sander, *Atmospheric Chemistry and Physics*, 2015, **15**, 4399–4981.